Research Square

Preprints are preliminary reports that have not undergone peer review.
They should not be considered conclusive, used to inform clinical practice,
or referenced by the media as validated information.

Hydroxylated metatitanic acid engineering of K2CO3/Al2O3 sorbents enables highly regenerable and cyclically stable CO2 capture

Mohammad Shahrzad Karkan
Iran University of Science and Technology
Amin Bazyari
abazyari@iust.ac.ir

Iran University of Science and Technology
Shahrokh Shahhosseini
Iran University of Science and Technology

Article

Keywords: CO2 capture, Potassium carbonate sorbent, Activated alumina, Metatitanic acid, Interfacial engineering, Regeneration

Posted Date: November 18th, 2026

DOI: https://doi.org/10.21203/rs.3.rs-11446996/v1

License: This work is licensed under a Creative Commons Attribution 4.0 International License.
Read Full License

Additional Declarations: No competing interests reported.

Hydroxylated metatitanic acid engineering of K_2CO_3/Al_2O_3 sorbents enables highly regenerable and cyclically stable CO_2 capture

Mohammad Shahrzad Karkan, Amin Bazyari*, Shahrokh Shahhosseini

School of Chemical, Petroleum, and Gas Engineering, Iran University of Science and Technology, P.O. Box 16765-163, Tehran, Iran

*Corresponding author. Tel./Fax: +98 21 7322 8755/ +98 21 7724 0496.

E-mail address: abazyari@iust.ac.ir (A. Bazyari).

Abstract

Carbonate-based solid sorbents are promising for low-temperature CO_2 capture, but their practical application is often hindered by incomplete regeneration and capacity loss arising from strong interactions between K_2CO_3 and alumina. Although titanium-containing modifiers have been investigated in related sorbents, the role of hydroxyl-rich metatitanic acid ($TiO(OH)_2$) in K_2CO_3/Al_2O_3 systems remains insufficiently established. Herein, K_2CO_3 was supported on high-surface-area active alumina derived from NH_4HCO_3-modified flash-calcined gibbsite and subsequently modified with hydroxyl-rich metatitanic acid ($TiO(OH)_2$) to engineer the carbonate–oxide interface. The modified alumina provided a high accessible surface area of 350 $m^2\ g^{-1}$, facilitating K_2CO_3 dispersion and interfacial modification. The optimized sorbent containing 20 wt% K_2CO_3 and 30 wt% metatitanic acid achieved a CO_2 adsorption capacity of 2.96 mmol g^{-1} at 20 °C and 7 bar, consistent with response surface model predictions. Metatitanic acid substantially reconstructed the porous structure, increasing the accessible surface area of K_2CO_3/Al_2O_3 from 114.7 to 243.7 $m^2\ g^{-1}$ while maintaining a highly dispersed carbonate phase. Equilibrium data were best described by the Freundlich model, indicating heterogeneous adsorption sites, while thermodynamic analysis revealed spontaneous and exothermic adsorption. Most importantly, metatitanic acid markedly enhanced regenerability, with an optimized regeneration condition of 140 °C for 40

min yielding ~99% regeneration efficiency. The optimized sorbent retained 96.5% of its initial capacity after ten adsorption–regeneration cycles. These results demonstrate that hydroxyl-rich metatitanic acid is an effective interfacial engineering strategy for developing regenerable and durable K_2CO_3/Al_2O_3 sorbents for low-temperature CO_2 capture.

Keywords: CO_2 capture, Potassium carbonate sorbent, Activated alumina, Metatitanic acid, Interfacial engineering, Regeneration.

1. Introduction:

The continuous increase in anthropogenic CO_2 emissions has intensified the need for effective carbon-mitigation strategies. Carbon capture is therefore being actively investigated as a complementary approach for reducing emissions from major stationary and industrial sources, particularly where direct emission reductions remain challenging [1,2]. Among the available capture technologies, adsorption using solid sorbents has attracted considerable interest because of its potential for high CO_2 uptake and selectivity, operational flexibility, and lower regeneration requirements than conventional liquid absorbents [3]. Nevertheless, the practical development of solid sorbents remains challenging because adsorption capacity, regeneration energy, cyclic stability, cost, and scalability must be simultaneously considered [4–6].

Aqueous amine scrubbing, particularly monoethanolamine (MEA)-based absorption, remains one of the most established technologies for post-combustion CO_2 capture owing to its rapid reaction kinetics and high absorption capacity [7]. However, solvent regeneration imposes a substantial energy penalty, with conventional MEA systems commonly requiring approximately 3.7–3.8 GJ t^{-1} CO_2, while oxidative and thermal degradation can cause solvent loss, degradation-product formation, and corrosion [8–11]. These limitations have stimulated interest in solid sorbents, including activated carbons, zeolites, metal–organic frameworks, mesoporous silicas, and chemically reactive alkaline materials [1,12,13]. Compared with

predominantly physisorptive materials, chemically reactive sorbents can provide stronger CO_2 interactions and potentially enable capture under moderate-temperature conditions [12]. Among them, alkali-metal carbonates are particularly attractive because of their relatively low cost, chemical stability, and reversible reaction with CO_2 in the presence of water vapor. Potassium carbonate (K_2CO_3) is one of the most extensively investigated alkali-carbonate sorbents. In the presence of water vapor, CO_2 reacts reversibly with K_2CO_3 to form potassium bicarbonate (R1):

$$K_2CO_3 + CO_2 + H_2O \rightleftharpoons 2KHCO_3 \quad \text{(R1)}$$

This reaction enables CO_2 capture at relatively low temperatures, while regeneration can occur at substantially lower temperatures than those typically required for calcium-based high-temperature looping systems [14,15]. The carbonation mechanism can also involve hydrated intermediate phases that influence reaction kinetics and reversibility [16]. However, unsupported K_2CO_3 suffers from limited accessibility of reactive sites and unfavorable mass-transfer characteristics. Supporting K_2CO_3 on a porous material can improve active-phase dispersion and accessibility while providing a more suitable structure for gas–solid contacting [17,18].

Among potential supports, Al_2O_3 has been widely investigated because of its high surface area, tunable porosity, mechanical strength, thermal stability, and relatively low cost [19,20]. K_2CO_3/Al_2O_3 sorbents can exhibit high CO_2 uptake and favorable carbonation kinetics; however, the interaction between the potassium phase and alumina can also introduce an important limitation. During carbonation and regeneration, potassium-containing species may interact with the alumina surface and form thermally stable potassium-aluminum carbonate hydroxide phases, which alter the carbonation-regeneration pathway and can hinder complete regeneration [21]. Zhao et al. reported high carbonation conversions of K_2CO_3/Al_2O_3 under moderate-temperature and humid conditions, while subsequent thermal analysis revealed

multiple decomposition stages associated with $KHCO_3$ and more stable potassium-aluminum carbonate species [22,23]. Other studies using bubbling and continuous fluidized-bed reactors have further demonstrated the potential of K_2CO_3/Al_2O_3 for practical CO_2 capture while showing that active-phase loading, water-vapor concentration, preparation method, and regeneration conditions strongly influence performance [24–28]. These findings establish K_2CO_3/Al_2O_3 as a promising sorbent platform but also highlight the need to control the active-phase/support interaction.

The formation of thermally stable potassium-aluminum carbonate hydroxide species, $KAl(CO_3)_2(OH)_2$, is particularly relevant to regeneration and cyclic stability. Such species are less readily decomposed than $KHCO_3$ and may contribute to incomplete regeneration and progressive capacity loss during repeated adsorption–desorption cycles [27,28]. The extent of potassium-alumina interaction depends on K_2CO_3 loading, support characteristics, preparation route, and operating conditions [24,27,28]. In addition, SO_2 and other flue-gas impurities can further affect the stability of potassium-based sorbents under realistic operating conditions [36]. Consequently, modifying the chemical environment at the carbonate–oxide interface represents a potentially effective strategy for controlling carbonation and regeneration behavior without abandoning the favorable characteristics of K_2CO_3/Al_2O_3.

Titanium-containing oxides provide a relevant basis for such interfacial modification. TiO_2 has previously been incorporated into K_2CO_3/Al_2O_3 and was reported to enhance the initial carbonation rate while maintaining stability within the investigated temperature range [37]. Related studies have also shown beneficial effects of Ti- and Zr-containing oxides in other alkali-carbonate systems, including improved desorption behavior and enhanced interfacial water activation [38,39]. These observations suggest that the chemical nature of the oxide surrounding the carbonate phase can influence both carbonation and regeneration. However,

anhydrous TiO_2 and hydroxylated titanium species may affect carbonate chemistry through different surface functionalities, particularly because hydroxyl groups can participate in water adsorption, dissociation, and proton-transfer processes.

Hydroxylated metal oxides are therefore of particular interest for improving carbonate decomposition. For example, $ZrO(OH)^+$ and $ZrO(OH)_2$ species have been reported to enhance CO_2 desorption kinetics, with experimental and first-principles studies indicating an important role of water adsorption and dissociation at hydroxylated oxide sites [40]. Metatitanic acid ($TiO(OH)_2$), a hydroxyl-rich titanium-containing material, has likewise demonstrated catalytic activity toward carbonate/bicarbonate decomposition. Dutcher et al. [41] reported that nanoporous $TiO(OH)_2$ reduced the activation energy for $NaHCO_3$ decomposition and enhanced CO_2 desorption in the $Na_2CO_3/NaHCO_3$ system, while subsequent studies further demonstrated the effectiveness of $TiO(OH)_2$-based materials for promoting CO_2 desorption [42]. These findings provide a mechanistic basis for considering metatitanic acid as an interfacial modifier in carbonate-based CO_2 sorbents.

More recently, metatitanic acid has been combined with Al_2O_3 aerogel for CO_2 capture, where its incorporation was associated with increased CO_2 uptake and reduced regeneration temperature and time [43]. However, that system differs fundamentally from K_2CO_3/Al_2O_3 because CO_2 capture in the latter involves reversible carbonate/bicarbonate chemistry in addition to surface adsorption. Thus, the effect of $TiO(OH)_2$ on a chemically active K_2CO_3/Al_2O_3 sorbent cannot be inferred directly from either TiO_2-modified K_2CO_3/Al_2O_3 or metatitanic-acid-containing alumina systems. In particular, the influence of metatitanic acid on the adsorption-regeneration behavior and cyclic stability of K_2CO_3/Al_2O_3 remains insufficiently established.

Accordingly, this study investigates metatitanic acid ($TiO(OH)_2$) as a hydroxylated titanium-based interfacial modifier for K_2CO_3/Al_2O_3 sorbents. K_2CO_3 was supported on high-surface-

area active alumina derived from NH_4HCO_3-modified flash-calcined gibbsite, and the effects of K_2CO_3 and metatitanic-acid loading on CO_2 capture were investigated. Response surface methodology was subsequently employed to determine the effects of adsorption temperature and pressure and to identify the optimum adsorption conditions. The optimized sorbent was further evaluated using adsorption isotherms, thermodynamic analysis, and structural and textural characterization. Finally, regeneration behavior and repeated adsorption-regeneration cycles were investigated to assess whether metatitanic-acid modification can improve the regenerability and cyclic stability of K_2CO_3/Al_2O_3 without presupposing a specific mechanism for potassium-alumina phase formation or suppression.

2. Materials and Methods

2.1. Chemicals

Flash-calcined gibbsite, used as the precursor for the preparation of high-surface-area active alumina, was kindly provided by Pars Pigment and Catalyst Co. Ammonium bicarbonate (NH_4HCO_3) was supplied by Daejung Chemicals & Metals Co., Ltd. Titanium isopropoxide (TTIP) was obtained from Sigma-Aldrich and used as the titanium precursor for metatitanic acid preparation. Potassium carbonate (K_2CO_3) and ethanol were purchased from Merck. Deionized water was used throughout the synthesis and preparation procedures. All chemicals were of analytical grade and used as received without further purification.

2.2. Preparation of adsorbents

2.2.1. Preparation of alumina support

The high-surface-area active alumina support was prepared from flash-calcined gibbsite using an NH_4HCO_3-assisted hydrothermal treatment. Briefly, 1.0 g of flash-calcined gibbsite and 1.5 g of NH_4HCO_3 were dispersed in 2.45 mL of deionized water. The suspension was stirred at 100 rpm for 30 min to obtain a homogeneous mixture. The resulting suspension was transferred to a Teflon-lined stainless-steel autoclave and hydrothermally treated at 70 °C for

15 h. After hydrothermal treatment, the solid was calcined at 400 °C for 1 h. The resulting material was ground using a mortar and pestle to obtain a homogeneous powder for subsequent impregnation.

2.2.2. Preparation of K_2CO_3/Al_2O_3 adsorbent

K_2CO_3/Al_2O_3 was prepared by wet impregnation. The required amount of K_2CO_3 was dissolved in deionized water under continuous stirring to obtain a homogeneous solution. The prepared active alumina support was then gradually added to the solution while stirring. The resulting suspension was maintained at 50 °C and stirred at 500 rpm for 4 h. The resulting slurry was dried at 100 °C for 24 h and subsequently calcined at 300 °C for 4 h in a conventional furnace. After calcination, the solid was ground to obtain a homogeneous K_2CO_3/Al_2O_3 powder.

2.2.3. Preparation of metatitanic acid

Metatitanic acid ($TiO(OH)_2$) was prepared by controlled hydrolysis of titanium isopropoxide (TTIP). Briefly, 6.0 mL of TTIP was combined with 6.9 mL of deionized water and stirred at 600 rpm for 4 h. The resulting precipitate was separated by centrifugation at 6000 rpm for 6 min. The precipitate was subsequently washed six times with ethanol and deionized water. The washed solid was dried at 100 °C for 24 h to obtain the metatitanic acid powder.

2.2.4. Preparation of metatitanic acid-modified K_2CO_3/Al_2O_3 adsorbent

Metatitanic-acid-modified K_2CO_3/Al_2O_3 was prepared by a wet mixing procedure. The required amount of metatitanic acid was dispersed in a known volume of deionized water under continuous stirring. The required amount of K_2CO_3/Al_2O_3 was then gradually added to the suspension. The resulting mixture was stirred at 60 °C and 600 rpm for 6 h to promote homogeneous incorporation of metatitanic acid. The resulting material was dried at 100 °C for 12 h and subsequently ground to obtain a homogeneous powder.

2.3. Characterization of materials

The crystalline structure of the synthesized samples was characterized by X-ray diffraction (XRD) using an Advance D8 diffractometer. The diffraction patterns were recorded over a 2θ range of 10-90°. Fourier transform infrared (FTIR) spectra were collected using a Spectrum RX-I spectrometer within the wavenumber range of 400-4000 cm^{-1} to identify the surface functional groups of the synthesized adsorbents. The textural properties, including the specific surface area, total pore volume, and average pore diameter, were determined by nitrogen adsorption-desorption measurements using a Mini2 surface area analyzer. Nitrogen was used as the adsorbate, and all measurements were performed at 77 K. The morphology of the synthesized samples was examined using a field-emission scanning electron microscope (FESEM, MIRA3, TESCAN) operated at an accelerating voltage of 15 kV.

2.4. CO_2 adsorption experiments

The CO_2 adsorption experiments were conducted using the experimental setup shown schematically in Fig. 1. Prior to each experiment, the gas preheating chamber and adsorption reactor were evacuated using a vacuum pump to remove residual gases. A predetermined amount of CO_2 was then introduced into the gas chamber to establish the desired initial pressure, while a thermostatic water circulator was used to maintain the adsorption system at the prescribed temperature. For each experiment, 0.5 g of the previously degassed sorbent was placed in the sorbent holder and positioned inside the adsorption reactor. After thermal equilibrium was established, the valve connecting the gas chamber to the adsorption reactor was opened to allow CO_2 to enter the adsorption cell. The adsorption experiment was continued for 60 min, which was determined to be sufficient to reach equilibrium under the investigated conditions. At the end of each experiment, the pressure and temperature of the system were recorded by the data-acquisition system and used to calculate the CO_2

adsorption capacity.

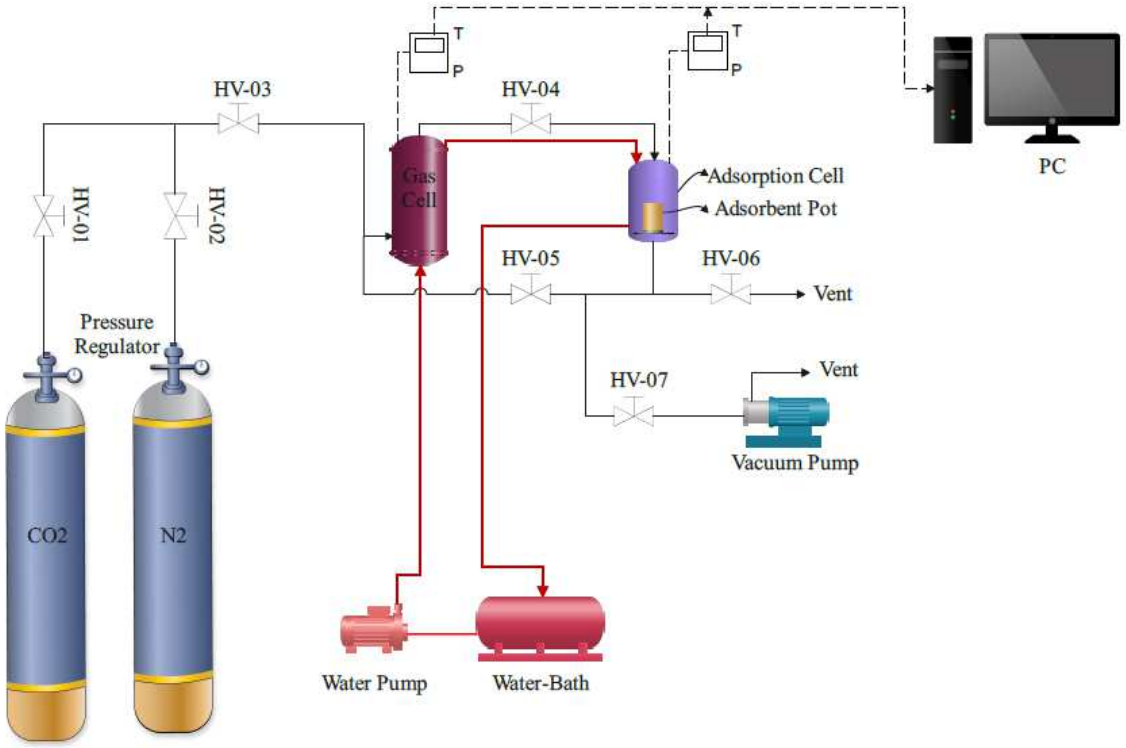


Fig. 1. Laboratory CO_2 adsorption system.

2.5. Calculation of CO_2 adsorption capacity

The CO_2 adsorption capacity of the synthesized adsorbents was calculated based on the difference between the amount of CO_2 present in the adsorption system before and after the adsorption process. The equilibrium adsorption capacity was obtained using Eq. (1):

$$q_t = \frac{n_i - n_f}{m_{ads}} \quad (1)$$

where q_t is the CO_2 adsorption capacity (mmol g^{-1}), n_i and n_f represent the initial and final amounts of CO_2 in the adsorption system (mmol), respectively, and m_{ads} is the mass of adsorbent used in the adsorption cell (g).

The amount of CO_2 at each measurement point was calculated using the real gas Eq. (2):

$$n = \frac{PV}{ZRT} \quad (2)$$

where P is the absolute pressure (bar), V is the free volume of the adsorption cell (L), Z is the compressibility factor, R is the universal gas constant (0.08314 L.bar.mol^{-1}.K^{-1}), and T is the absolute temperature (K). The free volume of the adsorption cell was considered as 58.04 cm^3. The cubic form of the Peng-Robinson equation was solved computationally (Eqs. 3 and 4) to determine the compressibility factor, and the largest real root corresponding to the gas phase was used in all adsorption capacity calculations.

$$P = \frac{RT}{v - b} - \frac{a(T)}{v(v + b) + b(v - b)} \tag{3}$$

$$Z^3 - (1 - B)Z^2 + (A - 2B - 3B^3)Z - (AB - B^2 - B^3) = 0 \tag{4}$$

2.6. Experimental design and response surface methodology (RSM)

The effects of adsorption temperature and pressure on the CO_2 adsorption capacity of the synthesized adsorbent were investigated using Response Surface Methodology (RSM). A Central Composite Design (CCD) was employed to develop the experimental design and establish the relationship between the operating variables and the adsorption performance. The experimental design and statistical analyses were carried out using Design-Expert software.

As shown in Table 1, adsorption temperature (20-60 °C) and pressure (1-7 bar) were selected as the independent variables, while the equilibrium CO_2 adsorption capacity (mmol g^{-1}) was considered as the response. A total of 13 experimental runs were generated according to the CCD matrix. The experimental data were fitted using a quadratic polynomial model, and the adequacy of the developed model was evaluated by analysis of variance (ANOVA). The statistical significance of the model terms was assessed at a confidence level of 95% ($p < 0.05$). Three-dimensional response surface plots and contour plots were generated to evaluate the interaction effects of the operating variables and to determine the optimum adsorption conditions.

Table 1. Experimental variables and their levels used in the CCD.

Factor	Name	Symbol	Type	Min	Max	Mean
Temperature (c)	T	A	Numeric	20	60	40
Pressure (bar)	P	B	Numeric	1	7	4

3. Results and discussion

3.1. N_2 adsorption-desorption

The textural properties and pore characteristics of the prepared adsorbents were investigated by N_2 adsorption-desorption analysis. The corresponding adsorption-desorption isotherms and BJH pore-size distribution curves are presented in Figs. 2 and 3, respectively, while the main textural parameters obtained from the BET analysis are summarized in Table 2:

Table 2. Textural properties of adsorbents.

Sample	BET surface area (m^2/g)	Mean pore diameter (nm)	Total pore volume (cm^3/g)
Al_2O_3	350	6.2	0.55
20KAl	115	6.2	0.18
30Ti20KAl	244	4.3	0.26

As shown in Fig. 2, all three samples exhibit a pronounced increase in the amount of adsorbed nitrogen at elevated relative pressures, accompanied by a hysteresis between the adsorption and desorption branches. This behavior, together with the pore-size distribution profiles presented in Fig. 3, is characteristic of a predominantly mesoporous structure[44]. The pore-size distribution curves show that the pore population is mainly concentrated within

the small-mesopore region, although a broader distribution extending toward larger pore diameters is also observed.

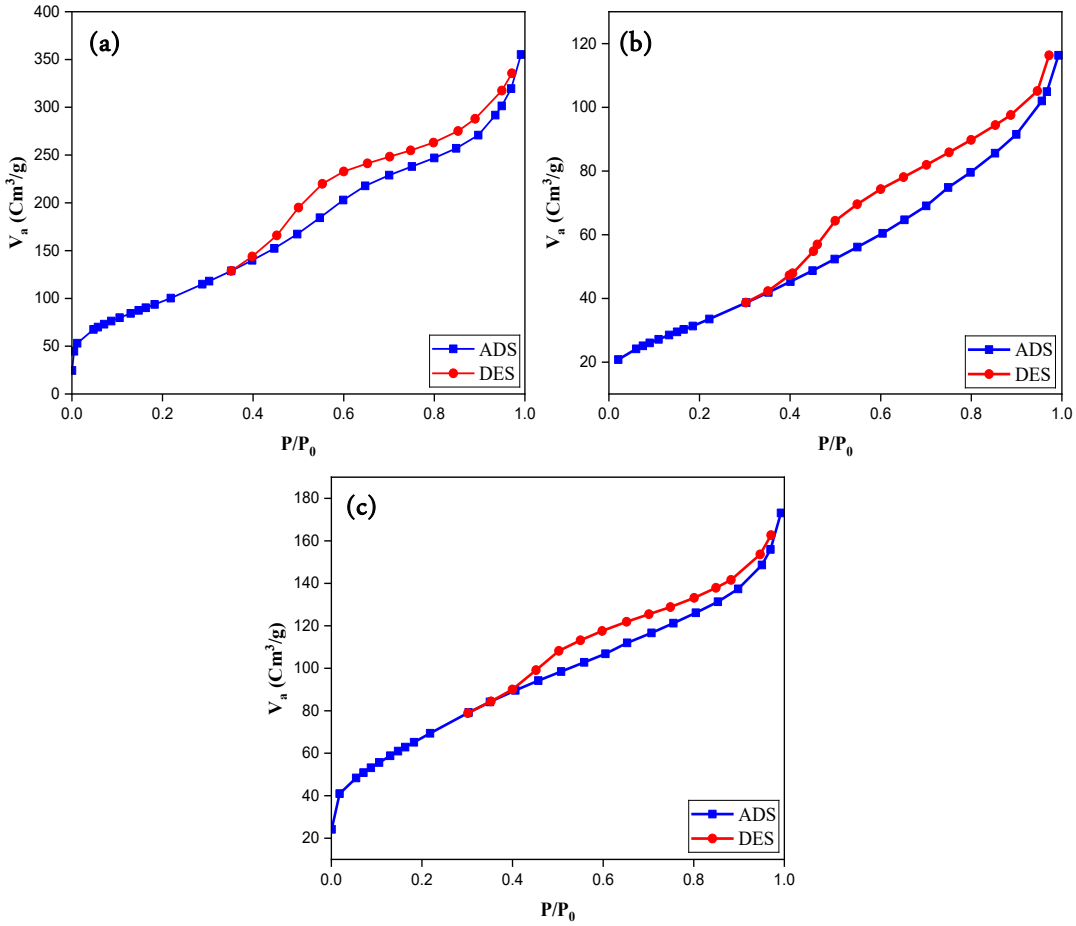


Fig. 2. Nitrogen adsorption-desorption isotherm curves of (a) alumina, (b) 20KAl, and (c) 30Ti20KAl samples.

The pristine alumina exhibited the highest nitrogen uptake among the investigated samples. Accordingly, it possessed the highest BET surface area and pore volume, with values of 350 $m^2\ g^{-1}$ and 0.55 $cm^3\ g^{-1}$, respectively. Its average pore diameter was 6.2 nm. The relatively high nitrogen uptake and well-developed pore structure indicate that the synthesized alumina provides a substantial accessible surface for subsequent incorporation of the active components.

A pronounced decrease in nitrogen uptake was observed after incorporation of K_2CO_3. As shown in Fig. 2(b), the adsorption-desorption isotherm of the 20KAl sample lies considerably below that of the pristine alumina over most of the relative-pressure range. Consistent with this observation, the BET surface area decreased from 350 to 115 m^2 g^{-1}, while the total pore volume decreased from 0.55 to 0.18 cm^3 g^{-1}. In contrast, the average pore diameter remained almost unchanged, decreasing only slightly from 6.2 to 6.2 nm. These changes suggest that K_2CO_3 loading substantially reduced the accessible porous surface, most likely because part of the porous structure became occupied or blocked by the supported potassium carbonate species [17].

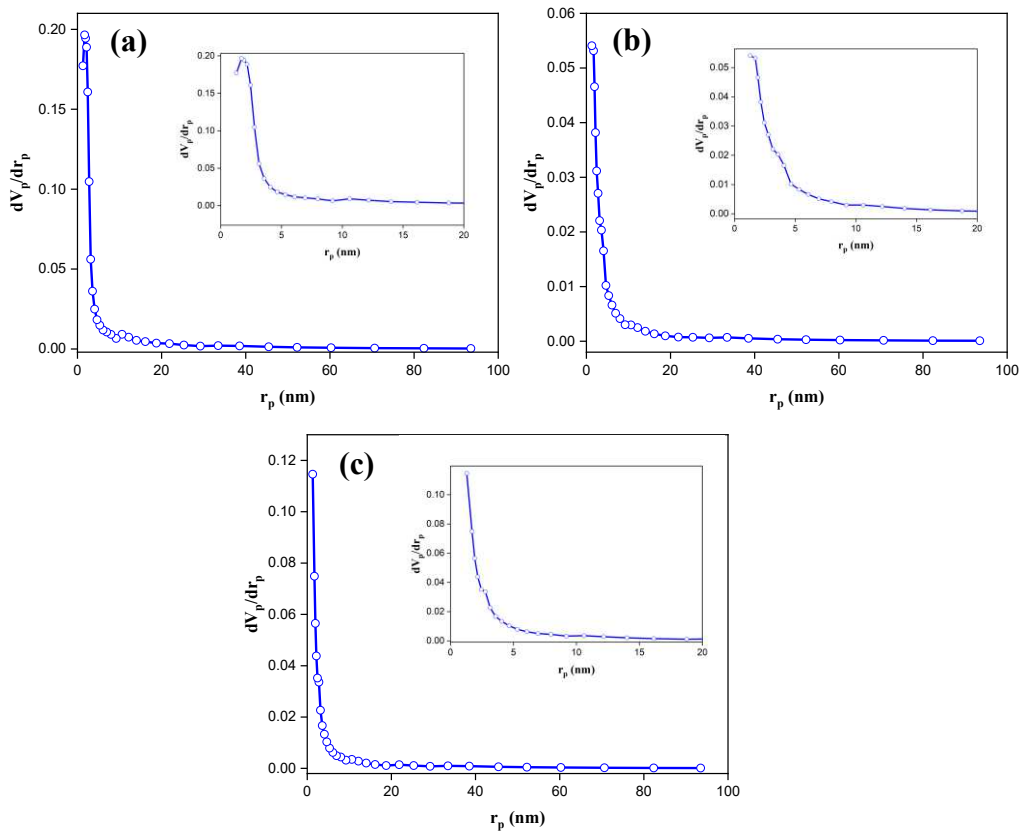


Fig. 3. Pore size distribution diagrams of (a) alumina, (b) 20KAl, and (c) 30Ti20KAL samples.

Following modification with metatitanic acid, the nitrogen uptake increased considerably compared with the 20KAl sample, as observed in Fig. 2(c). The BET surface area increased to 244 m^2 g^{-1} and the total pore volume increased to 0.26 cm^3 g^{-1}. At the same time, the average pore diameter decreased to 4.35 nm. The BJH distribution in Fig. 3(c) is also shifted toward smaller pore sizes compared with the corresponding distribution of the 20KAl sample. These changes indicate that metatitanic acid modification substantially altered the pore structure of the K_2CO_3-containing alumina and increased the accessible surface area, while producing a finer pore-size distribution.

The changes in monolayer adsorption capacity are consistent with the BET results. The V_m value decreased from 80 cm^3(STP) g^{-1} for pristine alumina to 26 cm^3(STP) g^{-1} after K_2CO_3 incorporation and subsequently increased to 56 cm^3(STP) g^{-1} after metatitanic acid modification. Similarly, the BET constant changed from 80 for pristine alumina to 105 for 20KAl and 80 for 30Ti20KAl. The recovery of V_m and surface area after metatitanic acid modification is consistent with the increased nitrogen uptake observed in the corresponding isotherm.

3.2. FTIR

FTIR spectroscopy was employed to investigate the surface chemical structure and to provide evidence for the incorporation of the active components into the alumina-based adsorbent. The FTIR spectra of pristine alumina, 20KAl, and 30Ti20KAl were recorded over the wavenumber range of 400-4000 cm^{-1} and are presented in Fig. 4.

The spectrum of pristine alumina shows a broad and relatively intense band in the range of 3400-3500 cm^{-1}, which can be attributed to the stretching vibrations of surface hydroxyl groups (O-H) and physically adsorbed water. The presence of this broad band indicates the hydroxylated nature of the alumina surface and the availability of surface hydroxyl sites. In addition, a band at approximately 1630 cm^{-1} is observed, which is assigned to the bending

vibration of H-O-H associated with adsorbed water molecules. In the lower-wavenumber region, characteristic bands in the range of 500-800 cm^{-1} are observed and are attributed to Al-O vibrations of the alumina framework [45]. The broad nature of these bands is consistent with the relatively low crystallinity of the synthesized alumina.

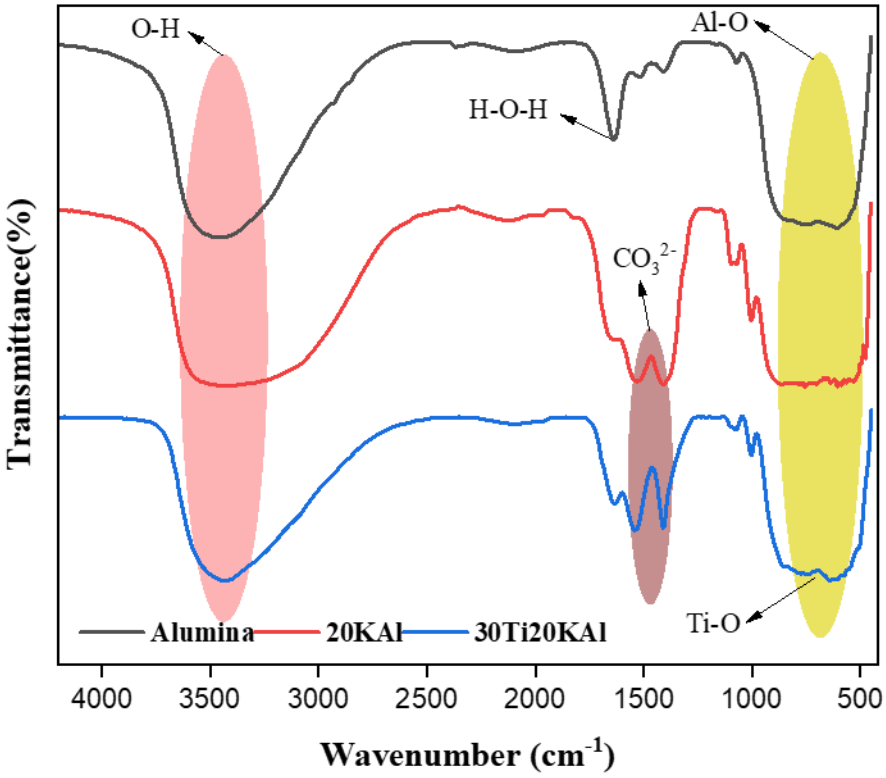


Fig. 4. FTIR spectra of the samples.

After incorporation of 20 wt% K_2CO_3, noticeable changes are observed in the FTIR spectrum. The most prominent change is the appearance of characteristic absorption bands associated with carbonate species in the 1400-1500 cm^{-1} region, which can be assigned to asymmetric stretching vibrations of CO_3^{2-}. Another absorption feature in the range of 1050-1100 cm^{-1} can be attributed to carbonate-related stretching vibrations [46]. The appearance of these characteristic bands provides spectroscopic evidence for the successful incorporation of K_2CO_3 into the alumina-based adsorbent. In addition, a decrease in the intensity of the broad

O-H band around 3400 cm^{-1} is observed after K_2CO_3 incorporation, suggesting a change in the surface hydroxyl environment. This change may be associated with interactions between carbonate species and hydroxyl groups on the alumina surface and may involve surface interactions such as Al-O-K species or ionic interactions between the carbonate-containing phase and the alumina surface [47].

Further spectral changes are observed after modification of 20KAl with 30 wt% metatitanic acid. In particular, the low-wavenumber region between approximately 500 and 700 cm^{-1} exhibits increased intensity and broadening compared with the corresponding spectrum of 20KAl. These changes can be associated with Ti-O- and Ti-O-Ti-related vibrations, providing evidence for the presence of the titanium-containing phase in the modified adsorbent [43]. The changes in the shape and breadth of this region may also indicate interactions between the titanium-containing phase and the alumina support. In this regard, the possible contribution of Ti-O-Al interactions cannot be excluded; however, such an assignment should be considered as an indication of interfacial interaction rather than direct proof of a specific Ti-O-Al bond based solely on FTIR analysis.

The carbonate-related absorption bands in the 1400-1500 cm^{-1} region also undergo changes in intensity and/or position after metatitanic acid modification. Such changes may arise from alterations in the local chemical environment of carbonate species following modification of the alumina surface. This observation suggests that the titanium-containing phase may influence the chemical environment of the supported K_2CO_3, indicating an interaction between the active carbonate phase and the modified support. Furthermore, the further decrease in the intensity of the O-H-related bands suggests additional changes in the surface hydroxyl environment during the modification process.

Overall, the FTIR results provide evidence for the successful incorporation of K_2CO_3 into the alumina support and the subsequent modification of the resulting adsorbent with metatitanic

acid. The characteristic bands associated with the alumina framework, carbonate species, and titanium-oxygen vibrations are simultaneously observed in the final 30Ti20KAl sample. The observed changes in the hydroxyl, carbonate, and low-wavenumber regions indicate that the modification process alters the surface chemical environment of the adsorbent. These chemical changes, together with the modifications in the textural properties observed from the BET analysis, may contribute to the enhanced CO_2 adsorption performance and improved regeneration behavior of the modified adsorbent.

3.3. XRD

The crystalline and structural characteristics of the prepared adsorbents were investigated by X-ray diffraction (XRD), and the corresponding diffraction patterns are presented in Fig. 5. The XRD patterns were recorded over a 2θ range of 10-90°. The results provide information regarding the structural characteristics of the alumina support and the changes induced by K_2CO_3 loading and subsequent metatitanic acid modification.

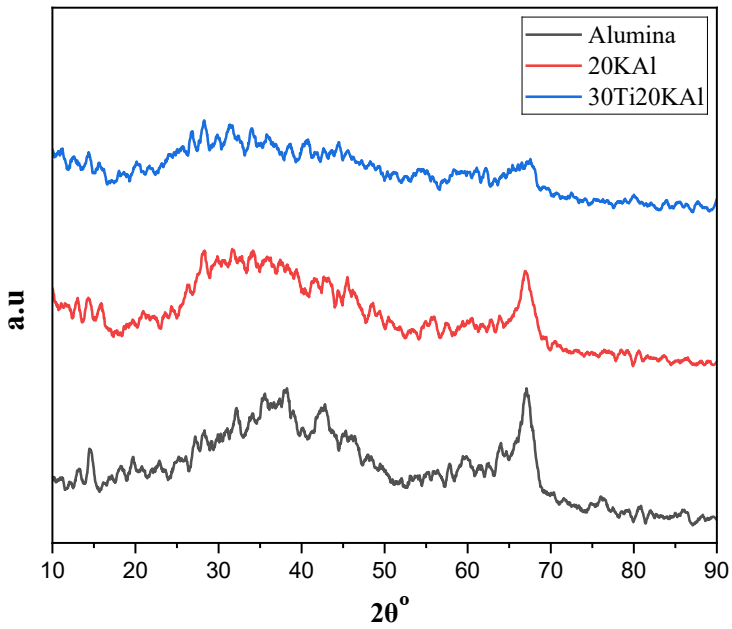


Fig. 5. XRD pattern of the samples.

The XRD pattern of pristine alumina is characterized by broad and relatively low-intensity diffraction features. A broad diffraction feature in the region of approximately 37-40° and a weaker feature around 66-68° can be assigned to the characteristic reflections of the alumina structure [48]. The broad nature of these diffraction features is indicative of small crystallite domains and a relatively low degree of long-range structural ordering in the synthesized active alumina.[48]. This observation is also consistent with the broad Al-O-related absorption bands observed in the FTIR spectrum.

Following the incorporation of 20 wt% K_2CO_3, the overall XRD pattern remains similar to that of the pristine alumina, with the characteristic alumina-related features retained at approximately the same angular positions [49]. This indicates that K_2CO_3 incorporation does not result in an obvious transformation of the alumina phase within the detection capability of XRD. Moreover, no distinct diffraction peaks attributable to a crystalline K_2CO_3 phase are observed. The absence of detectable K_2CO_3 reflections may indicate that the potassium carbonate is highly dispersed within the alumina structure, present predominantly in a poorly crystalline or amorphous state, and/or strongly associated with the support surface [49].

Further structural changes are observed after modification of the 20KAl sample with 30 wt% metatitanic acid. The modified sample exhibits broader diffraction features and an increased diffuse background, while the characteristic alumina-related features remain detectable. This behavior suggests an increase in structural disorder and a reduction in the apparent degree of crystallinity following modification. The absence of distinct additional crystalline reflections associated with a separate titanium-containing phase suggests that the titanium-containing component is either highly dispersed, poorly crystalline, or predominantly amorphous under the applied preparation and measurement conditions [43]. The reduction in the relative intensity of the characteristic alumina features may be associated with surface modification and the presence of the additional titanium-containing component.

Overall, the XRD results indicate that the alumina support maintains its basic structural characteristics after K_2CO_3 incorporation and subsequent metatitanic acid modification, while the latter treatments increase the structural disorder of the material. The absence of distinct crystalline phases corresponding to K_2CO_3 or the titanium-containing component suggests a highly dispersed and/or poorly crystalline nature of these components [43, 49]. These observations are in agreement with the FTIR results and support the successful modification of the alumina-based adsorbent without the formation of a clearly detectable separate crystalline phase.

3.4. SEM

Scanning electron microscopy (SEM) was employed to investigate the surface morphology and the changes induced by the incorporation of the active components into the alumina support. SEM images were obtained for pristine alumina, 20KAl, and 30Ti20KAl, and the corresponding micrographs are presented in Fig. 6. The SEM analysis was performed at an accelerating voltage of 15 kV.

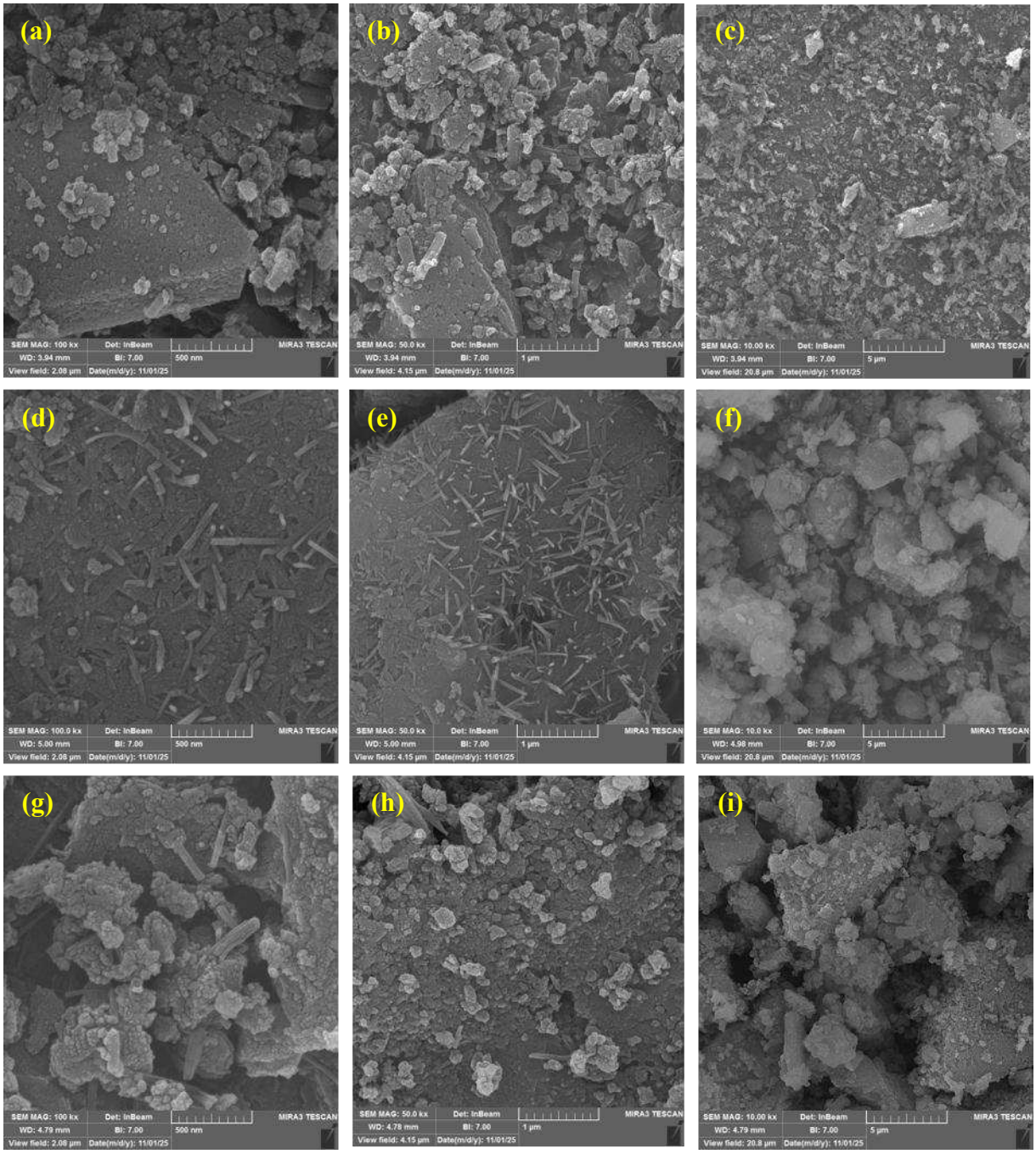


Fig. 6. SEM images of (a,b,c) pure alumina, (d,e,f) 20KAl, and (g,h,i) 30Ti20KAl samples.

The pristine alumina exhibits a relatively porous and heterogeneous surface morphology. The particles are predominantly irregular in shape and form moderately aggregated structures. At higher magnifications, fine particles can be observed on the surface of larger particles, indicating a heterogeneous surface texture. Interparticle voids and visible spaces are also

present in several regions of the sample, which are consistent with the relatively high surface area and pore volume obtained from the BET analysis.

Following the incorporation of 20 wt% K_2CO_3, a noticeable modification of the surface morphology is observed. The most prominent feature is the appearance of rod-like or needle-like structures distributed over the alumina surface. These morphological features are attributed to the deposited K_2CO_3-containing phase, consistent with the expected surface modification following impregnation of alumina with K_2CO_3. The structures appear to be distributed relatively uniformly over the observed regions, although some degree of aggregation is also evident. In addition, part of the surface voids observed in the pristine alumina appears to be covered by the deposited phase, which is consistent with the considerable decrease in BET surface area and pore volume after K_2CO_3 loading.

Further morphological changes are observed after modification of the 20KAl sample with 30 wt% metatitanic acid. The surface appears more compact and aggregated than that of the K_2CO_3-containing sample. Fine particles are observed as clustered structures over the alumina surface, and relatively uniform surface coverage can be identified in several regions. Moreover, the needle-like structures observed in the 20KAl sample become less pronounced after metatitanic acid modification. This change may be associated with the additional deposition and dispersion of the titanium-containing phase over the existing surface structures, resulting in partial coverage or modification of the previously observed K_2CO_3-related morphology.

The SEM observations are consistent with the textural changes obtained from the BET analysis. K_2CO_3 incorporation results in a substantial reduction in the accessible surface area and pore volume, which can be related to the partial coverage or occupation of the porous structure by the deposited active phase [30]. After metatitanic acid modification, the surface morphology becomes more compact and aggregated, while the BET surface area and pore

volume partially recover relative to the 20KAl sample. This indicates that the surface morphology and textural properties are significantly affected by the sequential incorporation of K_2CO_3 and metatitanic acid.

Overall, the SEM results demonstrate that the incorporation of K_2CO_3 and subsequent modification with metatitanic acid produce clear morphological changes in the alumina-based adsorbent. The observed evolution from the porous and irregular morphology of pristine alumina to the modified and more aggregated surface structures of 20KAl and 30Ti20KAl confirms that the preparation procedure substantially alters the surface characteristics of the adsorbent.

3.5. Optimization of adsorbent composition

The composition of the adsorbent plays a crucial role in determining its CO_2 adsorption performance. Therefore, prior to optimizing the operating conditions using Response Surface Methodology (RSM), a series of preliminary adsorption experiments was conducted to identify the optimum adsorbent composition. Initially, different potassium carbonate loadings were evaluated to determine the most suitable amount of the active phase. Subsequently, the adsorbent with the optimum potassium carbonate loading was further modified with different metatitanic acid contents. The adsorbent composition exhibiting the highest CO_2 adsorption capacity was selected for all subsequent characterization and optimization studies.

3.5.1. K_2CO_3 loading effect

The effect of K_2CO_3 loading on CO_2 adsorption capacity is shown in Fig. 7 Increasing the K_2CO_3 loading from 10 to 20 wt% enhanced the adsorption capacity from 0.73 to 1.03 mmol g^{-1}, whereas further loading resulted in a gradual decrease, reaching 0.61 mmol g^{-1} at 50 wt%. The initial improvement is attributed to the increased availability of active alkaline sites, while the subsequent decline is likely associated with pore blockage and K_2CO_3

agglomeration at higher loadings. Therefore, 20 wt% K_2CO_3 was selected as the optimum loading for subsequent modification with metatitanic acid.

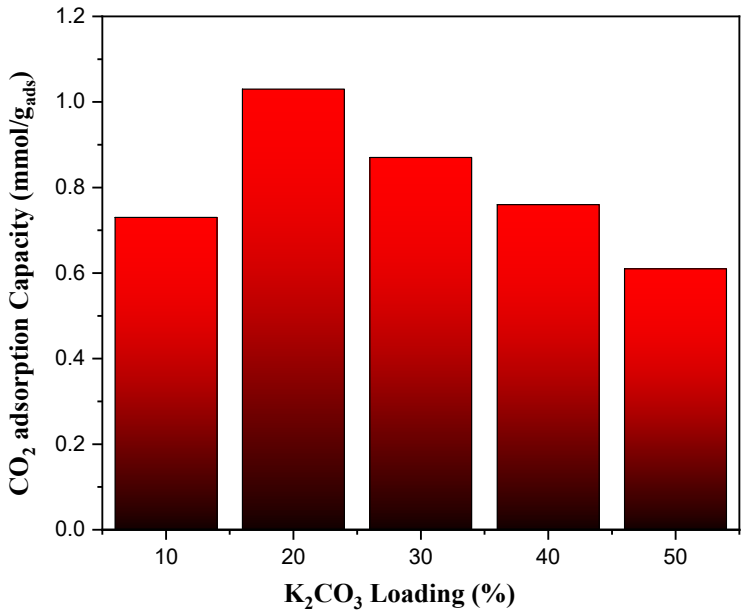


Fig. 7. Effect of K_2CO_3 loading on CO_2 adsorption capacity of adsorbents.

3.5.2. MTA loading effect

Increasing the metatitanic acid content from 10 to 30 wt% progressively increased the CO_2 adsorption capacity from 1.19 to 1.39 mmol g^{-1}, with the maximum capacity obtained at 30 wt% (Fig. 8). Further increasing the loading to 40 and 50 wt% decreased the capacity to 1.23 and 1.08 mmol g^{-1}, respectively. The improvement at moderate loadings can be attributed to favorable surface modification, improved accessibility of active sites, and enhanced dispersion of K_2CO_3 on the alumina support. In contrast, excessive metatitanic acid loading may cover the support surface and partially obstruct the pore structure, limiting active-site accessibility and CO_2 transport. Thus, 30 wt% metatitanic acid provided the optimum balance between surface modification and accessible porosity. Accordingly, the adsorbent containing 20 wt% K_2CO_3 and 30 wt% metatitanic acid was selected for subsequent optimization of adsorption temperature and pressure using Response Surface Methodology.

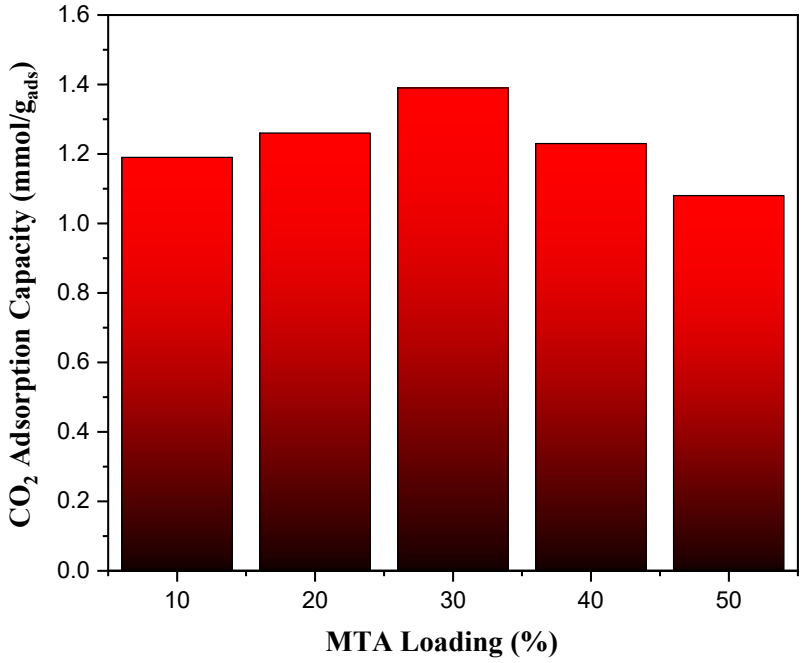


Fig. 8. Effect of MTA loading on CO_2 adsorption capacity of adsorbents.

3.6. RSM Results

3.6.1. Analysis of variance (ANOVA)

The results of the analysis of variance (ANOVA) for the quadratic model developed for CO_2 adsorption capacity are presented in Table 3. The model was evaluated using statistical parameters such as the F-value and p-value to assess its significance and reliability. The obtained F-value of 287.50 with a p-value of <0.0001 indicates that the model is highly significant. This confirms that the developed quadratic model adequately represents the relationship between the investigated operating variables and the CO_2 adsorption capacity within the experimental domain.

Table 3. ANOVA results for the RSM.

Source	Sum of squares	df	Mean square	F-value	p-value
Model	2.61	5	0.5224	287.50	<

					0.0001
A-T	0.6256	1	0.6256	344.31	<
					0.0001
B-P	1.94	1	1.94	1065.47	<
					0.0001
AB	0.0004	1	0.0004	0.2201	0.6532
A^2	0.0399	1	0.0399	21.95	0.0022
B^2	0.0016	1	0.0016	0.8637	0.3836
Residual	0.0127	7	0.0018		
Lack of Fit	0.0098	3	0.0033	4.47	0.0909
Pure Error	0.0029	4	0.0007		
Cor Total	2.62	12			

As shown in Table 3, both adsorption temperature (A) and pressure (B) are statistically significant linear terms, with p-values of <0.0001. Among these variables, pressure has a substantially greater contribution to the adsorption capacity, as evidenced by its higher F-value of 1065.47 compared with 344.31 for temperature. The quadratic temperature term (A^2) is also statistically significant (p = 0.0022), indicating the presence of a nonlinear effect of temperature on CO_2 adsorption capacity. In contrast, the interaction term between temperature and pressure (AB) is not statistically significant (p = 0.6532). Similarly, the quadratic pressure term (B^2) does not have a significant effect within the investigated range, with a p-value of 0.3836.

The statistical parameters related to the model fit are also presented in Table 4. The coefficient of determination (R^2) of 0.9952 indicates a very good agreement between the

calculated and experimental adsorption capacities, with 99.52% of the experimental variation being explained by the developed model. Furthermore, the adjusted R^2 of 0.9917 is in close agreement with the R^2 value, indicating that the model maintains a high explanatory capability after considering the number of model terms. The predicted R^2 value of 0.9729 also demonstrates the strong predictive capability of the model. The relatively small difference between the adjusted and predicted R^2 values further confirms the reliability of the model within the experimental domain.

Table 4. Results of fitting the quadratic model.

Parameter	Value
R^2	0.9952
Adjusted R^2	0.9917
Predicted R^2	0.9729
Adeq. Precision	55.4798
Std. Dev.	0.0426
Mean	1.74
C.V. %	2.45

The adequacy of the developed model was further evaluated using the lack-of-fit test. The obtained F-value of 4.47 and p-value of 0.0909 indicate that the lack-of-fit is not statistically significant, demonstrating that the deviation between the model predictions and the experimental data is not significant compared with the pure experimental error. In addition, the Adeq Precision value of 55.48 is substantially higher than the recommended value of 4, indicating a sufficient signal-to-noise ratio and confirming that the model can be reliably used for navigating the experimental design space. The coefficient of variation (CV) of 2.45% further indicates a relatively low dispersion of the experimental data around the mean

response. Therefore, the statistical results confirm that the developed quadratic model provides a reliable representation of the CO_2 adsorption behavior over the investigated temperature and pressure ranges.

3.6.2. Adsorption Model

Following confirmation of the model's validity and its satisfactory fit to the experimental data, the quadratic model presented in Eq. 5 was obtained to predict the adsorption capacity at different temperature and pressure conditions.

$$q_{CO2} = 2.26521 - 0.058879 \times T + 0.270536 \times P + 0.000667 \times T \times P + 0.000417 \times T^2 - 0.003678 \times P^2 \quad (5)$$

3.6.3. Diagnostic plots

The adequacy of the developed RSM model was further evaluated using the diagnostic plots shown in Fig. 9. The predicted versus actual plot shows a close agreement between the experimental and predicted values, with most points distributed near the 45° reference line. The normal probability plot indicates an approximately linear distribution of the residuals, suggesting no significant deviation from normality. In addition, the residuals versus run plot shows that the residuals are randomly distributed around zero and remain within the acceptable limits, with no apparent systematic trend. Overall, the diagnostic plots confirm the satisfactory adequacy and reliability of the developed quadratic model.

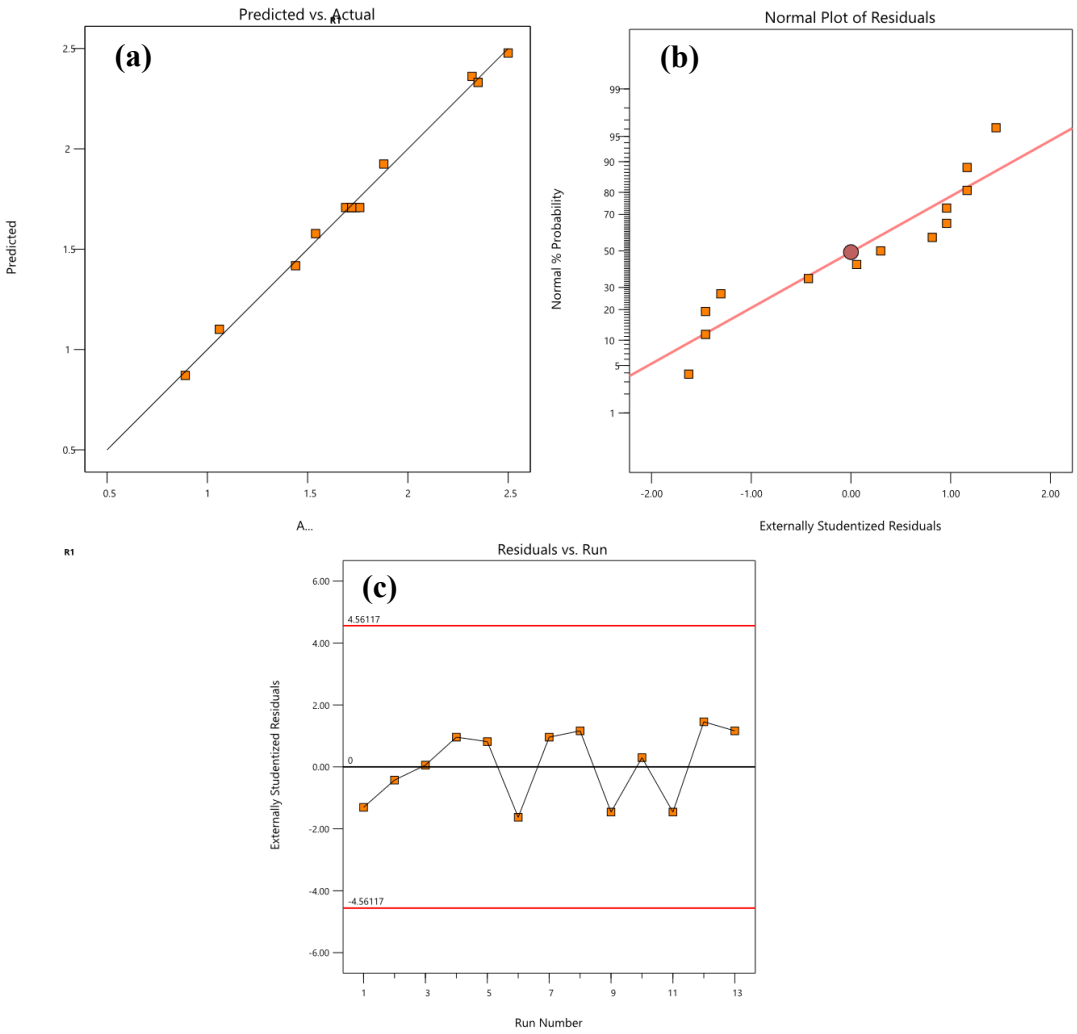


Fig. 9. (a) predicted versus actual plot, (b) normal probability plot of residuals, and (c) plot of residual versus number of runs for CO_2 adsorption capacity.

3.6.4. Effect of variables on CO_2 adsorption capacity

The effects of adsorption temperature and pressure on the CO_2 adsorption capacity are illustrated by the three-dimensional response surface and contour plot shown in Fig. 10. Both plots provide a clear representation of the variation in adsorption capacity within the investigated experimental region. The response surface indicates that CO_2 uptake generally increases with increasing pressure and decreases with increasing temperature. Accordingly, the higher adsorption capacities are located toward the region of higher pressure and lower temperature.

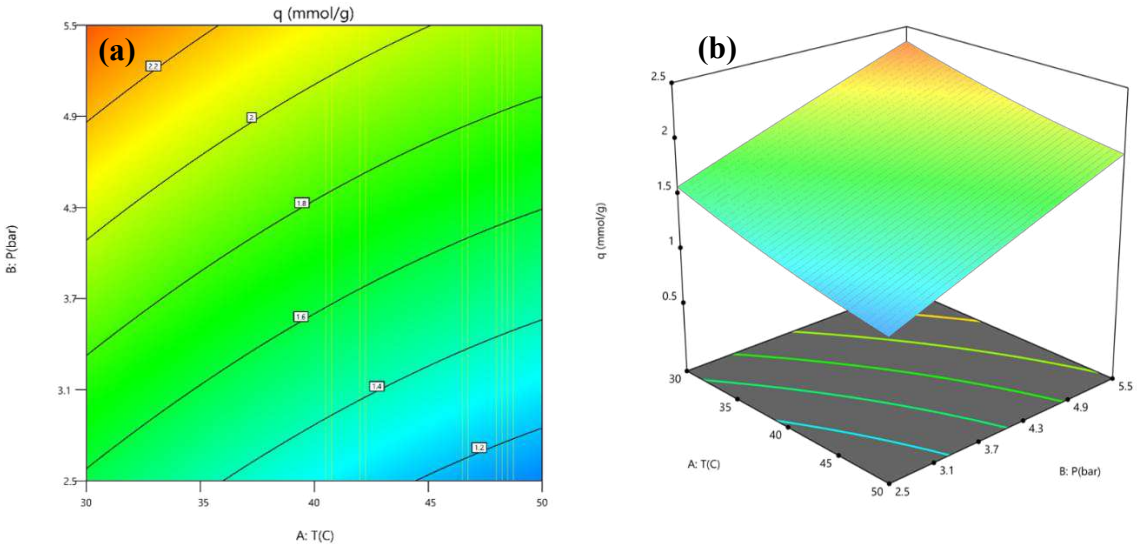


Fig. 10. (a) The 3D response surface plots of the temperature and pressure and (b) contour plot.

The contour plot further illustrates this behavior, with the response increasing from approximately 1.2 to 2.2 mmol g^{-1} across the displayed experimental region as the operating conditions shift toward higher pressure and lower temperature. The relatively regular and predominantly diagonal distribution of the contour lines indicates that the response is governed mainly by the individual effects of temperature and pressure, rather than by a pronounced interaction between the two factors. This observation is consistent with the ANOVA results, where both linear terms were highly significant ($p < 0.0001$), whereas the temperature–pressure interaction term (AB) was not statistically significant ($p = 0.6532$). The pronounced positive effect of pressure can be attributed to the increased partial pressure of CO_2, which enhances the driving force for mass transfer from the gas phase toward the adsorbent surface and promotes CO_2 uptake [50]. This trend is clearly supported by the experimental results. At 40 °C, increasing the pressure from 1 to 7 bar increased the adsorption capacity from 0.89 to 2.50 mmol g^{-1}. Similar pressure-dependent behavior was observed at other temperatures investigated in the CCD. In contrast, increasing temperature

generally decreased the adsorption capacity. At 4 bar, the adsorption capacity decreased from 2.35 mmol g^{-1} at 20 °C to an average of approximately 1.72 mmol g^{-1} at the central condition of 40 °C, and further decreased to 1.44 mmol g^{-1} at 60 °C. The decrease in CO_2 uptake with increasing temperature is consistent with the exothermic character of adsorption, for which increasing temperature can reduce the equilibrium affinity of the adsorbent toward CO_2 [50]. Overall, the response surface and contour plots confirm that pressure is the dominant operating variable within the investigated range, while temperature has a significant negative and nonlinear effect on CO_2 adsorption. The combined graphical and statistical analyses therefore indicate that higher pressure and relatively lower temperature favor CO_2 adsorption by the optimized adsorbent.

3.6.5. CO_2 adsorption conditions optimization

Numerical optimization was performed to determine the optimum operating conditions for maximizing CO_2 adsorption capacity within the investigated experimental ranges. as detailed in Table 5, The optimized conditions yielded a maximum predicted adsorption capacity of 3.1 mmol g^{-1} at a temperature of 20 °C and a pressure of 7 bar, with a desirability value of 0.9825, indicating highly favorable optimization conditions. A practical experiment was conducted under the optimized conditions to verify the accuracy of the numerical optimization and the predictive capability of the developed model. The experimental adsorption capacity was 2.96 mmol g^{-1}, showing good agreement with the predicted value. The difference between the predicted and experimental responses was 0.1014 mmol g^{-1}, corresponding to a relative deviation of approximately 3.4%. These results confirm the adequacy of the developed quadratic model and its capability to reliably predict CO_2 adsorption capacity within the investigated experimental domain.

Table 5. Optimization summary of CO_2 adsorption process parameters.

Name	Goal	Lower limit	Upper limit	Weight	Importance
Temperature	Is in range	20	60	1	3
Pressure	Is in range	1	7	1	3
Adsorption Capacity	Maximize	0.89	3.1	1	3

3.7. Adsorption isotherm

To investigate the equilibrium adsorption behavior of CO_2 and obtain further insight into the adsorption mechanism, the experimental equilibrium data were fitted using the Langmuir, Freundlich, and Dubinin–Radushkevich (D–R) isotherm models. These models were selected to evaluate the adsorption characteristics of the adsorbents, including surface homogeneity or heterogeneity and the characteristics of the adsorption equilibrium and adsorbate–adsorbent interactions [51]. The equilibrium adsorption experiments were conducted at 25 °C over the pressure range of 1-7 bar, and the resulting data were used for isotherm modeling. The isotherm parameters for each model were determined by nonlinear fitting using MATLAB software. In addition, the corresponding fitting parameters, including the coefficient of determination (R^2) and average absolute relative error (AARE), were calculated to evaluate the agreement between the experimental data and the predictions of the applied isotherm models.

As shown in Fig. 11(a), the equilibrium adsorption capacity of 20KAl increased progressively with increasing CO_2 pressure over the investigated pressure range. Among the three models, the Freundlich model provided the closest agreement with the experimental data throughout the pressure range, particularly at intermediate and relatively high pressures. The Langmuir model was also able to reproduce the general adsorption trend, although some deviation from

the experimental data was observed. In comparison, the D-R model exhibited a greater deviation from the experimental points, particularly at higher pressures.

For the 30Ti20KAl adsorbent (Fig. 11(b)), a higher adsorption capacity was observed compared with 20KAl over the investigated pressure range. This result indicates that modification of the K_2CO_3/alumina adsorbent with metatitanic acid favorably affected its CO_2 adsorption performance. Similar to 20KAl, the Freundlich model exhibited the best agreement with the experimental equilibrium data, whereas the Langmuir model provided a comparatively less accurate description. The D-R model showed the lowest statistical agreement among the three investigated models.

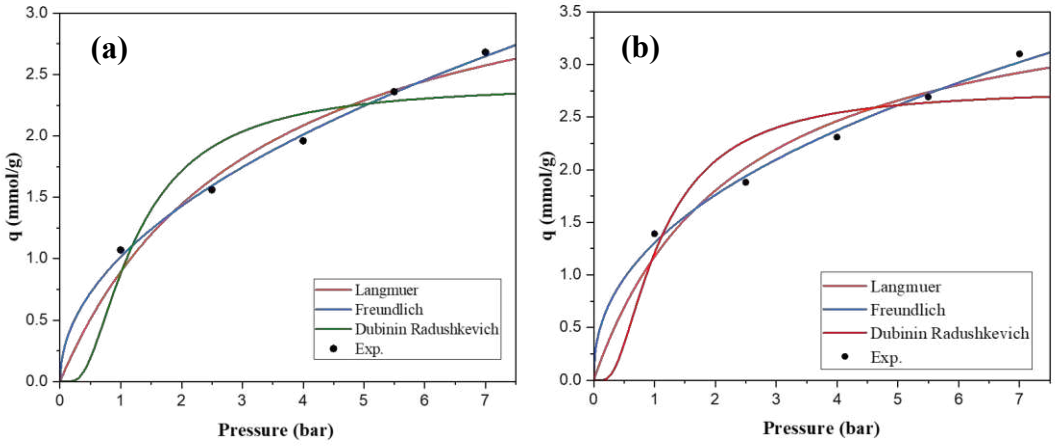


Fig. 11. Fitting of carbon dioxide adsorption isotherm models with experimental data: (a) 20% potassium carbonate on alumina and (b) 30% metatitanium on 20% potassium carbonate on alumina at 25°C.

The fitting parameters and statistical indicators for the three isotherm models are presented in Table 6. For the Langmuir model, the calculated maximum monolayer adsorption capacities (q_m) were 3.749 and 3.888 mmol g^{-1} for 20KAl and 30Ti20KAl, respectively. The corresponding Langmuir constants (K_L) were 0.313 and 0.432, respectively. The increase in both (q_m) and (K_L) following metatitanic acid modification suggests an improvement in the

apparent adsorption capacity and apparent affinity of the adsorbent toward CO_2. However, the (R^2) values of 0.9822 and 0.9679 and the AARE values of 0.06551 and 0.0741 obtained for 20KAl and 30Ti20KAl, respectively, indicate that the Langmuir model does not provide the most accurate representation of the experimental equilibrium data.

Table 6. Parameters of adsorption isotherms for the samples tested at 25°C.

Model	Equation	Parameter	20KAl	30Ti20KAl
Langmuir	$q_e = q_m K_l C/(1 + K_l C)$	q_m	3.749	3.888
		K_L	0.313	0.432
		R^2	0.9822	0.9679
		AARE	0.06551	0.0741
Freundlich	$q_e = K_F C^{(1/n_F)}$	K_F	1.015	1.304
		n_F	2.028	2.315
		R^2	0.9977	0.9940
		AARE	0.0228	0.0314
Dubinin Radushkevich	$q_e = q_m \exp(-\beta\varepsilon^2)$	q_m	2.423	2.767
		β	0.355	0.291
		ε	1.187	1.310
		R^2	0.8935	0.8764
		AARE	0.1350	0.1193

The Freundlich model exhibited the best statistical performance for both adsorbents. The calculated (K_F) values were 1.015 for 20KAl and 1.304 for 30Ti20KAl, while the corresponding (n_F) values were 2.028 and 2.315, respectively. The (n_F) values greater than unity are generally associated with favorable adsorption behavior [51]. Moreover, the high (R^2) values of 0.9977 and 0.9940, together with the low AARE values of 0.0228 and 0.0314

for 20KAl and 30Ti20KAl, respectively, demonstrate the superior ability of the Freundlich model to describe the experimental equilibrium data. The better performance of this empirical model suggests that the equilibrium adsorption behavior is more consistent with a heterogeneous distribution of adsorption sites with different energetic characteristics [51].

The D-R model was additionally applied to obtain information regarding the adsorption mechanism and the nature of the adsorbate-adsorbent interactions [52]. The calculated (q_m) values from this model were 2.423 and 2.767 mmol g^{-1} for 20KAl and 30Ti20KAl, respectively. The corresponding (β) values were 0.355 and 0.291, while the calculated mean adsorption energies (E) were 1.187 and 1.310 kJ mol^{-1}, respectively. The relatively low values of the mean adsorption energy are consistent with a predominantly physical adsorption mechanism [53]. However, the D-R model exhibited lower (R^2) values of 0.8935 and 0.8764 and higher AARE values of 0.1350 and 0.1193 for 20KAl and 30Ti20KAl, respectively, indicating that it provides a less satisfactory statistical description of the experimental equilibrium data compared with the Langmuir and Freundlich models.

Overall, the isotherm analysis demonstrates that the Freundlich model provides the most appropriate description of CO_2 equilibrium adsorption for both 20KAl and 30Ti20KAl. The combination of the highest (R^2) and lowest AARE values obtained for this model indicates that the equilibrium adsorption behavior is better represented by a heterogeneous surface model rather than an idealized homogeneous monolayer model. Furthermore, the low mean adsorption energies obtained from the D-R model support the predominance of physical interactions in the adsorption process. The higher (K_F), (q_m), and (K_L) values obtained after metatitanic acid modification further demonstrate the favorable effect of the modification on the CO_2 adsorption characteristics of the K_2CO_3/alumina-based adsorbent.

3.8. Adsorption thermodynamics

Thermodynamic analysis was performed to evaluate the feasibility and nature of CO_2 adsorption on the 20KAl and 30Ti20KAl adsorbents. The standard enthalpy change (ΔH°), standard entropy change (ΔS°), and standard Gibbs free energy change (ΔG°) were determined using the thermodynamic relationships described in Eqs. 6 and 7, based on the variation of ln (K_d) with the inverse of temperature (1/T) [54]. The thermodynamic parameters were evaluated at a pressure of 5.5 bar over the temperature range of 293-323 K, and the corresponding results are presented in Fig. 12 and Table 7.

$$\ln k_d = \frac{\Delta S^\circ}{R} - \frac{\Delta H^\circ}{RT} \quad (6)$$

$$\Delta G^\circ = \Delta H^\circ - T\Delta S^\circ \quad (7)$$

The ΔH° values for 20KAl and 30Ti20KAl were -6.644 and -7.144 kJ mol^{-1}, respectively. The negative values indicate the exothermic nature of CO_2 adsorption on both adsorbents. Moreover, the relatively low magnitudes of ΔH° are consistent with predominantly physical interactions between CO_2 and the adsorbent surface [55]. The slightly more negative ΔH° value for 30Ti20KAl suggests a somewhat stronger interaction between CO_2 molecules and the modified adsorbent.

The ΔS° values were -0.0027 and -0.0028 kJ mol^{-1} K^{-1} for 20KAl and 30Ti20KAl, respectively. The negative ΔS° values indicate a decrease in the configurational freedom of CO_2 molecules upon adsorption, which is associated with the transition from the relatively free gas phase to the more constrained adsorbed state [54].

As shown in Table 7, the calculated ΔG° values were negative over the entire investigated temperature range, confirming the thermodynamic favorability of CO_2 adsorption on both adsorbents. For 20KAl, ΔG° values ranged from -5.776 to -5.857 kJ mol^{-1}, while for 30Ti20KAl, they ranged from -6.243 to -6.327 kJ mol^{-1} as the temperature increased from 293 to 323 K. The more negative ΔG° values obtained for 30Ti20KAl indicate a more favorable Gibbs free-energy change for CO_2 adsorption.

Overall, the thermodynamic results confirm that CO_2 adsorption on both adsorbents is exothermic and thermodynamically favorable over the investigated temperature range. The more negative ΔH° and ΔG° values obtained for 30Ti20KAl indicate that metatitanic acid modification slightly strengthens the interaction between the adsorbent surface and CO_2 molecules, while the relatively low magnitude of ΔH° confirms that the adsorption remains predominantly physical in nature.

Table 7. Thermodynamic parameters of CO_2 adsorption.

Adsorbent	ΔH° (kJ.mol^{-1})	ΔS° (kJ.mol^{-1}K^{-1})	ΔG° (KJ.mol^{-1})			
			293	303	313	323
20KAl	-6.644	-0.0027	-5.857	-5.830	-5.803	-5.776
30Ti20KAl	-7.144	-0.0028	-6.327	-6.299	-6.271	-6.243

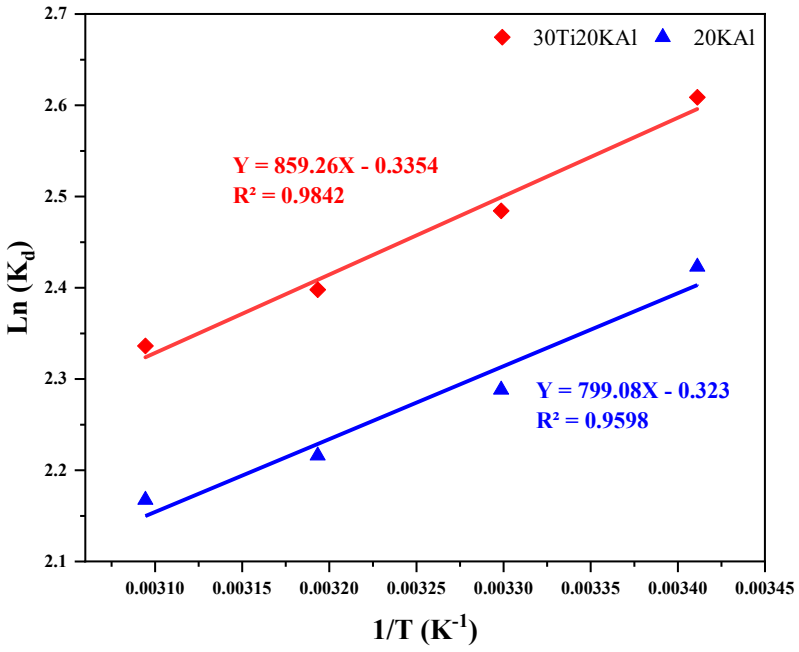


Fig. 12. The ln (K_d) vs. 1/T plot for CO_2 adsorption.

3.9. Regeneration performance and cyclic stability

3.9.1 Analysis of variance (ANOVA)

The regeneration conditions of the optimized 30Ti20KAl adsorbent were investigated using response surface methodology (RSM), with regeneration temperature and time as the independent variables and regeneration efficiency (R1) as the response. The ANOVA results are presented in Table 8. The developed quadratic model was statistically significant, indicating that the selected variables adequately described the regeneration behavior within the investigated experimental range. Regeneration temperature showed the strongest effect on R1, while regeneration time also had a significant effect. In contrast, the interaction between temperature and time was not statistically significant. The lack of fit was insignificant, confirming the adequacy of the model for describing the experimental data.

Table 8. Regeneration ANOVA results for the RSM.

Source	Sum of squares	df	Mean square	F-value	P-value
Model	573.42	5	114.68	17.58	0.0008
A-T	494.08	1	494.08	75.75	< 0.0001
B-P	60.75	1	60.75	9.31	0.0185
AB	6.25	1	6.25	0.9582	0.3602
A^2	6.18	1	6.18	0.9477	0.3627
B^2	9.51	1	9.51	1.46	0.2663
Residual	45.66	7	6.52		
Lack of Fit	34.86	3	11.62	4.30	0.0962
Pure Error	10.80	4	2.70		
Cor Total	619.08	12			

3.9.2 Regeneration Model

The final regression equation obtained in terms of the actual factors was expressed as (Eq. 8):

$$R = 1.55819 - 0.819971 \times T + 0.680819 \times t + 0.003125 \times T \times t + 0.001298 \times T^2 - 0.001511 \times t^2 \quad (8)$$

where R is the regeneration efficiency (%), (T) is the regeneration temperature (°C), and (t) is the regeneration time (min). The positive linear coefficients indicate that increasing temperature and time initially improves regeneration efficiency, whereas the negative quadratic terms indicate a tendency toward a maximum within the investigated range.

3.9.3 Diagnostic plots

The adequacy of the developed model was further evaluated using the diagnostic plots shown in Fig. 13. In the normal probability plot, the residuals are distributed approximately along the reference line, indicating an acceptable normal distribution of the residuals. Furthermore, the predicted versus actual plot shows a relatively close agreement between the experimental and predicted regeneration efficiencies. The absence of a pronounced systematic deviation from the diagonal line confirms the satisfactory predictive capability of the developed model within the studied range.

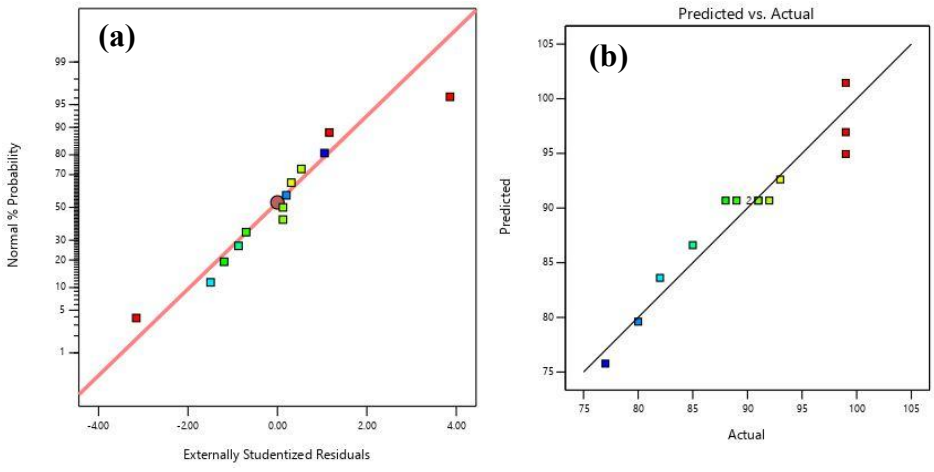


Fig. 13. (a) Predicted versus actual plot and (b) normal probability plot of residuals.

3.9.4 Effect of regeneration temperature and time

The effects of regeneration temperature and time on regeneration efficiency are illustrated by the response surface and contour plots in Fig. 14. Regeneration efficiency increased mainly with increasing temperature, confirming that temperature was the dominant factor identified by the ANOVA. Increasing regeneration time also improved the response, although its effect was less pronounced than that of temperature. At relatively high temperatures, extending the regeneration time resulted in only a limited additional improvement in regeneration efficiency. This behavior indicates that sufficiently high regeneration efficiency can be achieved without excessive regeneration time or temperature.

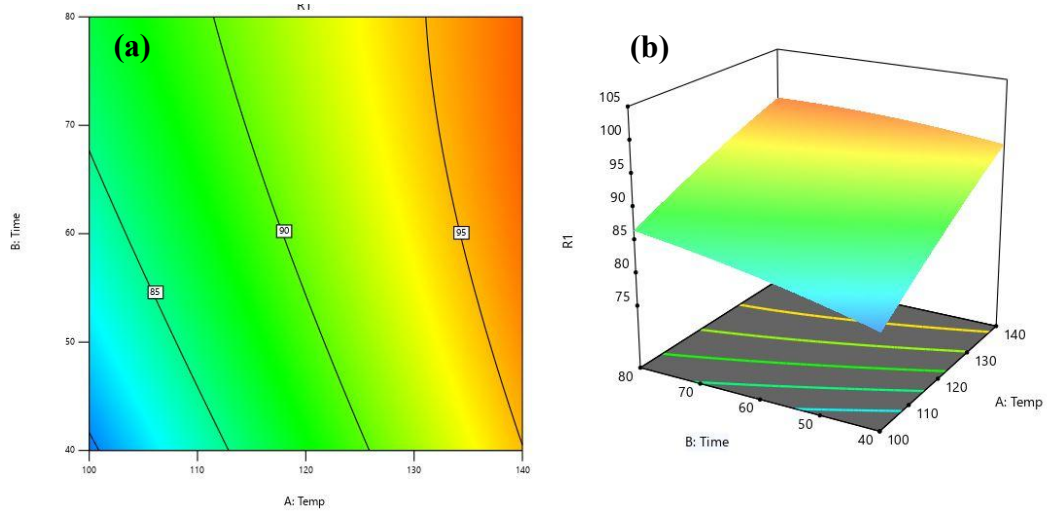


Fig. 14. (a) The 3D response surface plots of the temperature and pressure and (b) contour plot.

3.9.5 Optimization of regeneration conditions

The optimization results showed that a regeneration efficiency of approximately 99% could be achieved under several operating conditions. Among the high-efficiency solutions, regeneration at 140 °C for 40 min provided approximately 99% regeneration efficiency. Similar efficiencies were obtained at longer regeneration times or higher temperatures.

Therefore, 140 °C and 40 min were selected as the optimum regeneration conditions, as they provide high regeneration efficiency while minimizing both regeneration temperature and time. These conditions were subsequently used for the cyclic stability experiments.

3.9.6 Cyclic stability

The cyclic stability of the optimized 30Ti20KAl adsorbent was evaluated over ten consecutive adsorption-regeneration cycles under the selected regeneration conditions of 140 °C and 40 min. As shown in Fig. 15, the CO_2 adsorption capacity decreased only slightly from 1.42 mmol g^{-1} in the first cycle to 1.37 mmol g^{-1} after the tenth cycle. Thus, approximately 96.5% of the initial adsorption capacity was retained after ten cycles. The limited capacity loss demonstrates the good reversibility and cyclic stability of the adsorbent under repeated thermal regeneration, supporting its potential for repeated CO_2 capture applications.

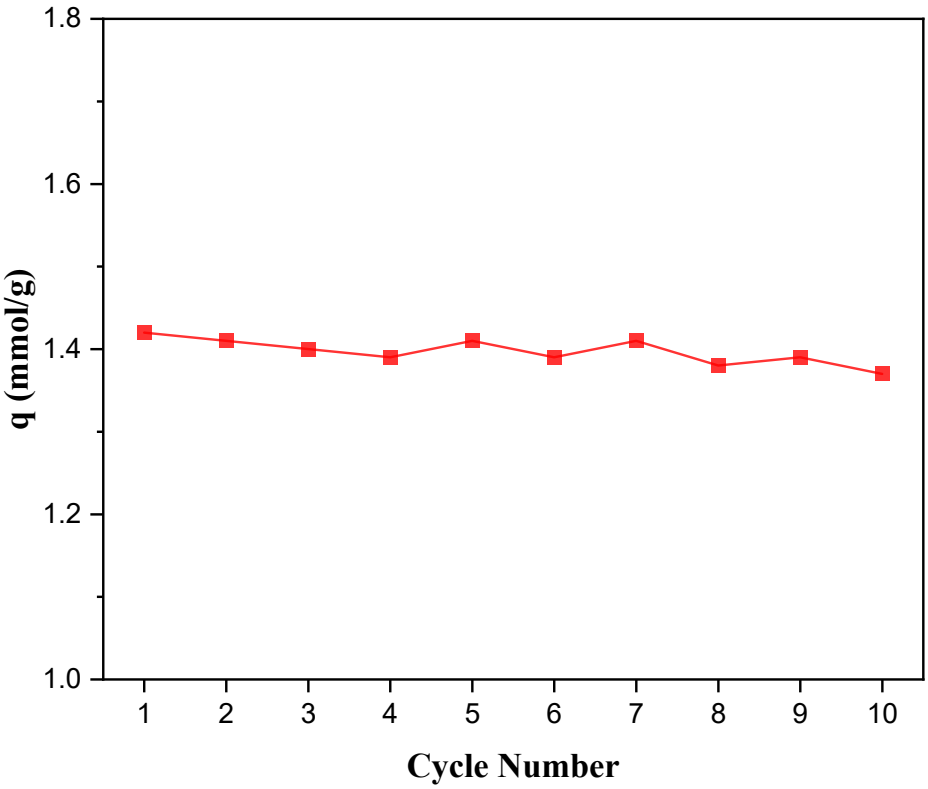


Fig. 15. Cycle stability of the optimized 30Ti20KAl adsorbent.

4. Conclusions

In this study, a K_2CO_3/Al_2O_3 adsorbent was prepared and subsequently modified with metatitanic acid to improve its CO_2 adsorption and regeneration performance. The effect of K_2CO_3 loading on the adsorption capacity was initially investigated, and 20 wt% K_2CO_3 was selected as the optimum loading. Subsequently, different amounts of metatitanic acid were incorporated into the selected K_2CO_3/Al_2O_3 adsorbent, and 30 wt% metatitanic acid was selected as the optimum modifier loading based on the preliminary adsorption experiments. The prepared samples were characterized using XRD, FTIR, BET, and SEM analyses. The BET surface area decreased from 350 m^2/g for the active alumina support to 115 m^2/g after K_2CO_3 loading, whereas modification with 30 wt% metatitanic acid increased the surface

area to 244 m^2/g. These changes indicate a substantial alteration of the pore structure following K_2CO_3 loading and subsequent metatitanic acid modification.

The CCD response surface methodology was employed to optimize the adsorption temperature and pressure. The results indicated that pressure was the dominant parameter affecting CO_2 adsorption capacity, while temperature had a negative nonlinear effect. The optimum adsorption conditions were determined as 20 °C and 7 bar, at which the model predicted a CO_2 adsorption capacity of 3.061 mmol/g. Experimental validation under these conditions yielded an adsorption capacity of 2.96 mmol/g, corresponding to a relative deviation of approximately 3.4% from the model prediction. Equilibrium adsorption data at 25 °C were better described by the Freundlich model for both 20KAl and 30Ti20KAl, indicating heterogeneous adsorption sites.

Thermodynamic analysis showed negative ΔH° values of -6.644 and -7.144 kJ/mol for 20KAl and 30Ti20KAl, respectively, confirming the exothermic nature of CO_2 adsorption. The negative ΔG° values obtained over the investigated temperature range indicated that CO_2 adsorption was thermodynamically favorable. The relatively low magnitude of ΔH° suggests weak overall CO_2 sorbent interactions, while the carbonate-based capture mechanism may also involve reversible chemical interactions. Regeneration experiments performed using response surface methodology showed that regeneration temperature was the most influential parameter, whereas regeneration time had a secondary effect. The selected regeneration condition was 140 °C for 40 min, at which a regeneration efficiency of approximately 99% was achieved. Finally, the optimized 30Ti20KAl adsorbent retained approximately 96.5% of its initial CO_2 adsorption capacity after 10 consecutive adsorption–regeneration cycles, with the capacity decreasing from 1.42 to 1.37 mmol/g. These results demonstrate that metatitanic acid modification can provide a modest improvement in the CO_2 adsorption capacity of K_2CO_3/Al_2O_3 while maintaining high regeneration efficiency and good cyclic stability.

Acknowledgments

This research did not receive dedicated funding from public, commercial, or nonprofit organizations.

Data availability

All data generated or analysed during this study are included in this published article.

References

1. Zentou H, Aliyu M, Abdalla MA, Abdelaziz OY, Hoque B, Alloush AM, et al. Advancements and challenges in adsorption-based carbon capture technology: from fundamentals to deployment. The Chemical Record. 2025;25(1):e202400188.
2. Paltsev S, Morris J, Kheshgi H, Herzog H. Hard-to-Abate Sectors: The role of industrial carbon capture and storage (CCS) in emission mitigation. Applied Energy. 2021;300:117322.
3. Karimi M, Shirzad M, Silva JA, Rodrigues AE. Carbon dioxide separation and capture by adsorption: a review. Environmental chemistry letters. 2023;21(4):2041-84.
4. Raganati F, Miccio F, Ammendola P. Adsorption of carbon dioxide for post-combustion capture: a review. Energy & Fuels. 2021;35(16):12845-68.
5. Zhang Y, Ding L, Xie Z, Zhang X, Sui X, Li J-R. Porous sorbents for direct capture of carbon dioxide from ambient air. Chinese Chemical Letters. 2025;36(3):109676.
6. Boer DG, Langerak J, Pescarmona PP. Zeolites as selective adsorbents for CO_2 separation. ACS Applied Energy Materials. 2023;6(5):2634-56.
7. Jiang W, Lin Y, Sun C, Sun Y, Zhu Y. Comparative review for enhancing CO_2 capture efficiency with mixed amine systems and catalysts. Molecules. 2024;29(19):4618.
8. Ren L, Cheng S, Xie T, Zhang Q, Li R, Yue T, et al. Low-energy regeneration technologies for industrial CO_2 capture: Advances, challenges, and engineering applications. Sustainability. 2025;17(21):9796.

9. Yuan B, Zhan G, Chen Z, Li Y, Wang L, You C, et al. Intrinsic insight of energy-efficiency optimization for CO_2 capture by amine-based solvent: effect of mass transfer and solvent regeneration. International Journal of Greenhouse Gas Control. 2022;118:103673.
10. Gouedard C, Picq D, Launay F, Carrette P-L. Amine degradation in CO_2 capture. I. A review. International journal of greenhouse gas control. 2012;10:244-70.
11. Peeters W, Neerup R, Fosbøl PL. Solvent degradation & influences on amine-based carbon capture operations. International Journal of Greenhouse Gas Control. 2025;147:104500.
12. Khan MFH, Ahmed I, Shovon SM, Akash FA, Leon TI, Rahman MA, et al. Advances in sustainable solid adsorbent materials for CO_2 capture: mechanisms, performance, and techno-economic perspectives. International Journal of Green Energy. 2026;23(9):1841-78.
13. Mouctar MH, Hassan MG, Bimbo N, Abbas SZ, Shigidi I. Comparative assessment and deployment of zeolites, MOFs, and activated carbons for CO_2 capture and geological sequestration applications. Inventions. 2025;10(5):78.
14. Guo Y, Sun J, Wang R, Li W, Zhao C, Li C, et al. Recent advances in potassium-based adsorbents for CO_2 capture and separation: a review. Carbon Capture Science & Technology. 2021;1:100011.
15. Pastrafidou M, Avraam K, Kartsonakis I. Carbon Capture and Storage in Waste-to-Energy Plants. 2026.
16. Luo H, Chioyama H, Thürmer S, Ohba T, Kanoh H. Kinetics and structural changes in CO_2 capture of K_2CO_3 under a moist condition. Energy & Fuels. 2015;29(7):4472-8.

17. Erto A, Balsamo M, Paduano LP, Lancia A, Di Natale F. Utilization of alumina-supported K_2CO_3 as CO_2-selective sorbent: A promising strategy to mitigate the carbon footprint of the maritime sector. Journal of CO_2 Utilization. 2018;24:139-48.

18. Erto A, Balsamo M, Lancia A, Di Natale F. Exploring the cyclic use of potassium carbonate supported on alumina for CO_2 capture in waterborne transport. Separation and Purification Technology. 2025;361:131481.

19. Kazemi H, Shahhosseini S, Bazyari A, Amiri M. A study on the effects of textural properties of γ-Al_2O_3 support on CO_2 capture capacity of Na_2CO_3. Process Safety and Environmental Protection. 2020;138:176-85.

20. Xiong L, Xu Z, Liu D, Ma J, Chen X. Preparation of K_2CO_3/γ-Al_2O_3 adsorbents for CO2 capture by spray fluidization impregnation granulation method. Fuel. 2026;407:137395.

21. Qin C, Yin J, Ran J, Zhang L, Feng B. Effect of support material on the performance of K2CO3-based pellets for cyclic CO_2 capture. Applied energy. 2014;136:280-8.

22. Zhao C, Chen X, Zhao C. K_2CO_3/Al_2O_3 for capturing CO_2 in flue gas from power plants. Part 1: Carbonation behaviors of K_2CO_3/Al_2O_3. Energy & fuels. 2012;26(2):1401-5.

23. Zhao C, Chen X, Zhao C. K_2CO_3/Al_2O_3 for capturing CO_2 in flue gas from power plants. Part 2: regeneration behaviors of K_2CO_3/Al_2O_3. Energy & fuels. 2012;26(2):1406-11.

24. Zhao C, Chen X, Zhao C, Wu Y, Dong W. K_2CO_3/Al_2O_3 for capturing CO_2 in flue gas from power plants. Part 3: CO_2 capture behaviors of K_2CO_3/Al_2O_3 in a bubbling fluidized-bed reactor. Energy & Fuels. 2012;26(5):3062-8.

25. Wu Y, Chen X, Dong W, Zhao C, Zhang Z, Liu D, et al. K_2CO_3/Al_2O_3 for capturing CO_2 in flue gas from power plants. Part 5: carbonation and failure behavior of

K_2CO_3/Al_2O_3 in the continuous CO_2 sorption–desorption system. Energy & fuels. 2013;27(8):4804-9.

26. Sengupta S, Amte V, Das AK, Yadav M, Mandal S, Nerivetla S, et al. Circulating fluid-bed studies for CO_2 capture from flue gas using K_2CO_3/Al_2O_3 adsorbent. Energy & Fuels. 2018;32(8):8594-604.

27. Sengupta S, Reddy SA, Dongara R, Das AK, Bhunia H, Bajpai PK. Improvement in regeneration properties and multicycle stability for K_2CO_3/Al_2O_3 adsorbents for CO_2 removal from flue gas. Energy & Fuels. 2014;28(8):5354-62.

28. Sengupta S, Amte V, Dongara R, Das AK, Bhunia H, Bajpai PK. Effects of the adsorbent preparation method for CO_2 capture from flue gas using K_2CO_3/Al_2O_3 adsorbents. Energy & Fuels. 2015;29(1):287-97.

29. Han J, Qin C, Gao C, Wang X, Ni J, Ran J. Monolithic K_2CO_3 adsorbent supported on honeycomb cordierite for Low-Temperature CO_2 capture. Separation and Purification Technology. 2025;376:134037.

30. Veselovskaya JV, Lysikov AI, Netskina OV, Kuleshov DV, Okunev AG. K_2CO_3-containing composite sorbents based on thermally modified alumina: synthesis, properties, and potential application in a direct air capture/methanation process. Industrial & Engineering Chemistry Research. 2020;59(15):7130-9.

31. Jansuda W, Phianchana K, Nokpho P, Chalermsinsuwan B, Potiyaraj P, Prasittisopin L. A Study of CO_2 Adsorption of MEA-Modified Zeolite 13X and K_2CO_3-Impregnated Alumina for Direct Air Capture. ACS omega. 2026;11(24):35750.

32. Gao Y, Yao Y, Zhao C, Huang P, Guo Y, Sun J. Amine modified potassium-based composite adsorbents prepared by spray granulation method for enhanced CO_2 capture performance. Separation and Purification Technology. 2025:134423.

33. Zheng J, Chen X, Ma J, Liang C. Characterization of the carbonation reaction of potassium-based composite adsorbents for direct air capture of CO_2. Separation and Purification Technology. 2025;363:132099.

34. Boonprasop S, Sangteerasintop S, Chalermsinsuwan B, Piumsomboon P. Optimum operating parameters of CO_2 sorption in turbulent fluidized bed regime using potassium carbonate supported on gamma alumina solid sorbent. RSC advances. 2018;8(69):39678-90.

35. Ryu D-Y, Jo S, Kim T-Y, In S-Y, Woo J-H, Lee J-H, et al. CO_2 sorption and regeneration properties of K_2CO_3/Al_2O_3-based sorbent at high pressure and moderate temperature. Applied Sciences. 2022;12(6):2989.

36. Omodolor IS, Otor HO, Andonegui JA, Allen BJ, Alba-Rubio AC. Dual-function materials for CO_2 capture and conversion: a review. Industrial & Engineering Chemistry Research. 2020;59(40):17612-31.

37. Dong W, Chen X, Wu Y. TiO_2-doped K_2CO_3/Al_2O_3 sorbents for CO_2 capture. Energy & fuels. 2014;28(5):3310-6.

38. Xu Z, Ma J, Chen X, Song Z, Liu D, Liang C. CO_2 capture performance of ZrO_2-doped Na_2CO_3/γ-Al_2O_3 adsorbent. Journal of Environmental Sciences. 2025;155:382-94.

39. Qi Z, Chen X, Xu Z, Liu Z, Ma J, Zhang F, et al. Study on direct air capture using Ti-doped K_2CO_3/ZrO_2 composite adsorbent: A combination of experimental, characterization and first-principles calculations. Chemical Engineering Journal. 2026:175943.

40. Wu Y, Cai T, Zhao W, Chen X, Liu H, Wang Y, et al. First-principles and experimental studies of $[ZrO(OH)]^+$ or $ZrO(OH)_2$ for enhancing CO_2 desorption kinetics–imperative

for significant reduction of CO_2 capture energy consumption. Journal of Materials Chemistry A. 2018;6(36):17671-81.

41. Dutcher B, Fan M, Leonard B. Use of multifunctional nanoporous $TiO(OH)_2$ for catalytic $NaHCO_3$ decomposition-eventually for $Na_2CO_3/NaHCO_3$ based CO_2 separation technology. Separation and purification technology. 2011;80(2):364-74.

42. Yao H, Toan S, Huang L, Fan M, Wang Y, Russell AG, et al. $TiO(OH)_2$–highly effective catalysts for optimizing CO_2 desorption kinetics reducing CO_2 capture cost: A new pathway. Scientific reports. 2017;7(1):2943.

43. Shokri A, Shahhosseini S, Bazyari A. Nanoporous Metatitanic acid on γ-Al_2O_3 aerogel for higher CO_2 adsorption capacity and lower energy consumption. Scientific Reports. 2024;14(1):22905.

44. Sing KS. Reporting physisorption data for gas/solid systems with special reference to the determination of surface area and porosity (Recommendations 1984). Pure and applied chemistry. 1985;57(4):603-19.

45. Rutkowska I, Marchewka J, Jeleń P, Odziomek M, Korpyś M, Paczkowska J, et al. Chemical and structural characterization of amorphous and crystalline alumina obtained by alternative sol–gel preparation routes. Materials. 2021;14(7):1761.

46. Weilach C, Spiel C, Föttinger K, Rupprechter G. Carbonate formation on Al_2O_3 thin film model catalyst supports. Surface science. 2011;605(15-16):1503-9.

47. Kantschewa M, Albano EV, Etrtl G, Kno H. Infrared and x-ray photoelectron spectroscopy study of K_2CO_3/γ-Al_2O_3. Applied catalysis. 1983;8(1):71-84.

48. Urbonavicius M, Varnagiris S, Pranevicius L, Milcius D. Production of gamma alumina using plasma-treated aluminum and water reaction byproducts. Materials. 2020;13(6):1300.

49. Veselovskaya JV, Derevschikov VS, Kardash TY, Stonkus OA, Trubitsina TA, Okunev AG. Direct CO_2 capture from ambient air using K_2CO_3/Al_2O_3 composite sorbent. International Journal of Greenhouse Gas Control. 2013;17:332-40.

50. Zhou D-D, Zhang X-W, Mo Z-W, Xu Y-Z, Tian X-Y, Li Y, et al. Adsorptive separation of carbon dioxide: From conventional porous materials to metal–organic frameworks. EnergyChem. 2019;1(3):100016.

51. Danat BT, Wuana RA, Chahul HF, Iorungwa MS. Review of adsorption isotherms models. Applied Water Science. 2026;16(3):72.

52. Shimizu S, Matubayasi N. Adsorbate-adsorbate interactions on microporous materials. Microporous and Mesoporous Materials. 2021;323:111254.

53. Zheng H, Liu D, Zheng Y, Liang S, Liu Z. Sorption isotherm and kinetic modeling of aniline on Cr-bentonite. Journal of hazardous materials. 2009;167(1-3):141-7.

54. Mansouri K, Ghaemi A. Exploring the Potential of KOH-Modified MXene ($Ti_3C_2T_x$) as a Promising Adsorbent for Enhanced CO_2 Capture. Sustainable Chemistry for Climate Action. 2026:100227.

55. Naderi K, Ghaemi A. Zinc Ferrite/Amine-Functionalized reduced graphene oxide nanocomposites for High-Efficiency CO_2 separation. Separation and Purification Technology. 2025;360:130980.